IL-13–programmed airway tuft cells produce PGE$_2$, which promotes CFTR-dependent mucociliary function

Maya E. Kotas,[1] Camille M. Moore,[2,3] Jose G. Gurrola II,[4] Steven D. Pletcher,[4,5] Andrew N. Goldberg,[4] Raquel Alvarez,[1] Sheyla Yamato,[1] Preston E. Bratcher,[6,7] Ciaran A. Shaughnessy,[6] Pamela L. Zeitlin,[6,7] Irene H. Zhang,[8] Yingchun Li,[2] Michael T. Montgomery,[2] Keehoon Lee,[8] Emily K. Cope,[8] Richard M. Locksley,[9,10] Max A. Seibold,[2,6,11] and Erin D. Gordon[1]

[1]Division of Pulmonary, Critical Care, Allergy and Sleep Medicine, Department of Medicine, University of California, San Francisco, San Francisco, California, USA. [2]Center for Genes, Environment, and Health, National Jewish Health, Denver, Colorado, USA. [3]Department of Biostatistics and Informatics, University of Colorado, Aurora, Colorado, USA. [4]Department of Otolaryngology - Head and Neck Surgery, University of California, San Francisco, San Francisco, California, USA. [5]Surgical Service, ENT Section, San Francisco VA Medical Center, San Francisco, California, USA. [6]Department of Pediatrics, National Jewish Health, Denver, Colorado, USA. [7]Department of Pediatrics, University of Colorado Anschutz Medical Center, Aurora, Colorado, USA. [8]Center for Applied Microbiome Sciences, Pathogen and Microbiome Institute, Northern Arizona University, Flagstaff, Arizona, USA. [9]Howard Hughes Medical Institute and [10]Department of Medicine, University of California, San Francisco, San Francisco, California, USA. [11]Division of Pulmonary Sciences and Critical Care Medicine, Department of Medicine, University of Colorado, Aurora, Colorado, USA.

Chronic type 2 (T2) inflammatory diseases of the respiratory tract are characterized by mucus overproduction and disordered mucociliary function, which are largely attributed to the effects of IL-13 on common epithelial cell types (mucus secretory and ciliated cells). The role of rare cells in airway T2 inflammation is less clear, though tuft cells have been shown to be critical in the initiation of T2 immunity in the intestine. Using bulk and single-cell RNA sequencing of airway epithelium and mouse modeling, we found that IL-13 expanded and programmed airway tuft cells toward eicosanoid metabolism and that tuft cell deficiency led to a reduction in airway prostaglandin E$_2$ (PGE$_2$) concentration. Allergic airway epithelia bore a signature of PGE$_2$ activation, and PGE$_2$ activation led to cystic fibrosis transmembrane receptor–dependent ion and fluid secretion and accelerated mucociliary transport. These data reveal a role for tuft cells in regulating epithelial mucociliary function in the allergic airway.

Introduction

Chronic rhinosinusitis with nasal polyps (CRSwNP) and asthma are common airway diseases characterized by persistent type 2 (T2), or "allergic," inflammation. The 2 diseases share a number of genetic risk loci (1, 2), and patients with disease affecting the upper airway have more severe lower airway symptoms, consistent with overlapping pathologic mechanisms (3). A key finding in both conditions is the IL-13–induced shift in epithelial cell type composition in favor of mucus secretory cells (goblet cells) with resultant pathologic secretions. Although IL-13 has also been shown to alter the transcriptional profile and function of all common airway epithelial cell types (basal, secretory, ciliated) (4), functional shifts in rare cells are incompletely described.

The airway epithelium is composed of prevalent cell types such as basal, ciliated, and secretory/mucus cells, interspersed with rare cell types such as neuroendocrine cells, ionocytes, and tuft cells. These rare cells, while technically challenging to interrogate, are increasingly recognized for their contributions to airway homeostasis and mucosal immunity. For example, the discovery of ionocytes in human and mouse trachea revealed that these are the highest expressers of cystic fibrosis transmembrane receptor (CFTR), an ion channel important in regulating the composition of airway surface liquid and maintaining bacterial host defense (5, 6). Neuroendocrine cells can sense and protect against hypoxia (7), as well as augment T2 inflammation through effects on type 2 innate lymphoid cells (8). Tuft cells initiate and amplify T2 inflammation in the mouse intestine (9–11) and can stimulate protective reflexes such as cough or apnea, as well as inflammation, in the airway (12, 13).

The full range of tuft cell outputs and functions, particularly in human disease, remains poorly understood. In addition to IL-25, mouse tuft cells are capable of producing leukotrienes, prostaglandins, and acetylcholine, suggesting potentially pleiotropic roles in tissue homeostasis. Although recent studies have suggested that tuft cells may be a source of IL-25 in nasal polyposis (14, 15) and activate T2 immunity as in the mouse intestine, perturbations of tuft cells in human airway disease have not been fully explored. Existing atlases of the cellular landscape in CRSwNP and allergic asthma that have broadly examined immune, stromal, and epithelial cells have not identified these rare but potentially important cells (16, 17). With this in mind, we sought to identify and phenotype tuft cells in the human respiratory epithelium and to explore their role in the pathobiology of allergic airway disease.

Results

Tuft cells expand and adopt an "allergic" transcriptional program of eicosanoid metabolism in nasal polyps. To define the cellular composition of human allergic (T2 inflamed) sinus tissue, we collected epithelial brushes from ethmoid-based polyps of 5 patients with CRSwNP or from healthy ethmoid tissue of 4 controls (Supplemental Table 1; supplemental material available online with this article; https://doi.org/10.1172/jci.insight.159832DS1) and subjected dissociated cells to single-cell RNA sequencing (scRNA-Seq). Initial clustering of 116,358 epithelial cells (Supplemental Figure 1A) revealed 15 distinct clusters, each including cells from all patients (Supplemental Table 2). Cluster identities were assigned based on expression of previously described cell type markers (Supplemental Figure 1B) and then aggregated based on similar expression profiles into 10 cell types: basal, proliferating basal, "hillock" basal (6, 17), supra-basal, early secretory, secretory, mucus secretory (goblet), ciliated, and a rare cell type cluster containing markers of both ionocytes and tuft cells (Figure 1A and Supplemental Table 3). We found a similar percentage of most cell types between patients with polyps and controls, suggesting a largely preserved cellular composition (Supplemental Figure 1C). We did, however, observe an overrepresentation of mucus secretory (goblet) cells with high expression of both *MUC5AC* and *MUC5B* in polyp epithelium, consistent with the mucus metaplasia observed in patients with CRSwNP (18) (Supplemental Figure 1C and Supplemental Table 2).

Subclustering of the rare cell type cluster identified both tuft cells (expressing *POU2F3*, *ASCL2*, and *AVIL*) and ionocytes (expressing *CFTR*, *ASCL3*, and *FOXI1*) (Figure 1, B and C, and Supplemental Figure 1D), whereas neuroendocrine cells were not found. The cytokine *IL25*, characteristically produced by mouse tuft cells, was not detectable in human tuft cells, consistent with prior reports (19, 20). While ionocyte frequencies did not differ with disease (median 1.7% vs. 1.2%, Figure 1D, Supplemental Table 2), we observed approximately 2.5-fold more tuft cells in polyps compared with healthy sinus (0.2% vs. 0.53%, Figure 1D and Supplemental Table 2). The presence of tuft cells and ionocytes (Supplemental Figure 1E) and the increase in tuft cells (Figure 1E) were confirmed by in situ RNA hybridization in histologic sections from control and nasal polyp tissue.

We next explored whether the expression profile of tuft cells was altered in polyp patients. Comparing tuft cells to all other cell types, we identified a set of tuft cell markers common to both polyp patients and controls, including *ASCL2*, *POU2F3*, and *AVIL*, which we call "common markers." Then, comparing tuft cells from control versus polyp patients, we identified a second set of genes increased in the tuft cells of polyp patients, including *BMX*, *GNG13*, *TRPM5*, and *PTGS1*, which we call "polyp tuft markers" (Figure 1F). All the tuft cells from healthy participants and a subset of those from polyp patients expressed only common tuft markers. The remaining tuft cells in polyp patients, which we called "allergic" tuft cells, expressed both common and polyp tuft markers. Polyp tuft markers were uniquely enriched for genes associated with the arachidonic acid metabolic pathway, including both *PTGS1* and *ALOX5* (Figure 1, G–I; Supplemental Figure 1, F and G; and Supplemental Figure 2, A and B). We compared our 2 tuft cell phenotypes (healthy and allergic) to publicly available tuft cell transcriptomic profiles. Healthy human sinus tuft cells resembled previous descriptions of human airway tuft cells (19, 20), while canonical markers of mouse tuft cells (21) such as *TRPM5* and *DCLK1* were present only in the allergic tuft cell population in polyp patients (Supplemental Figure 2C). Markers for previously described subsets of small intestinal or airway mouse tuft cells (6, 22) did not discriminate between healthy and allergic human airway tuft cells (Supplemental Figure 2D).

Pan-epithelial gene signatures in nasal polyps are imparted by IL-13 and prostaglandin E_2. CRSwNP is mediated by T2 inflammation, with a prominent role for IL-13 (16). Although many genes have altered expression in the setting of T2 inflammation, prior work identified a simplified 3-gene signature of T2 inflammation in the bronchial and nasal epithelium of asthmatics that correlates with clinical phenotype (23, 24).

JCI INSIGHT
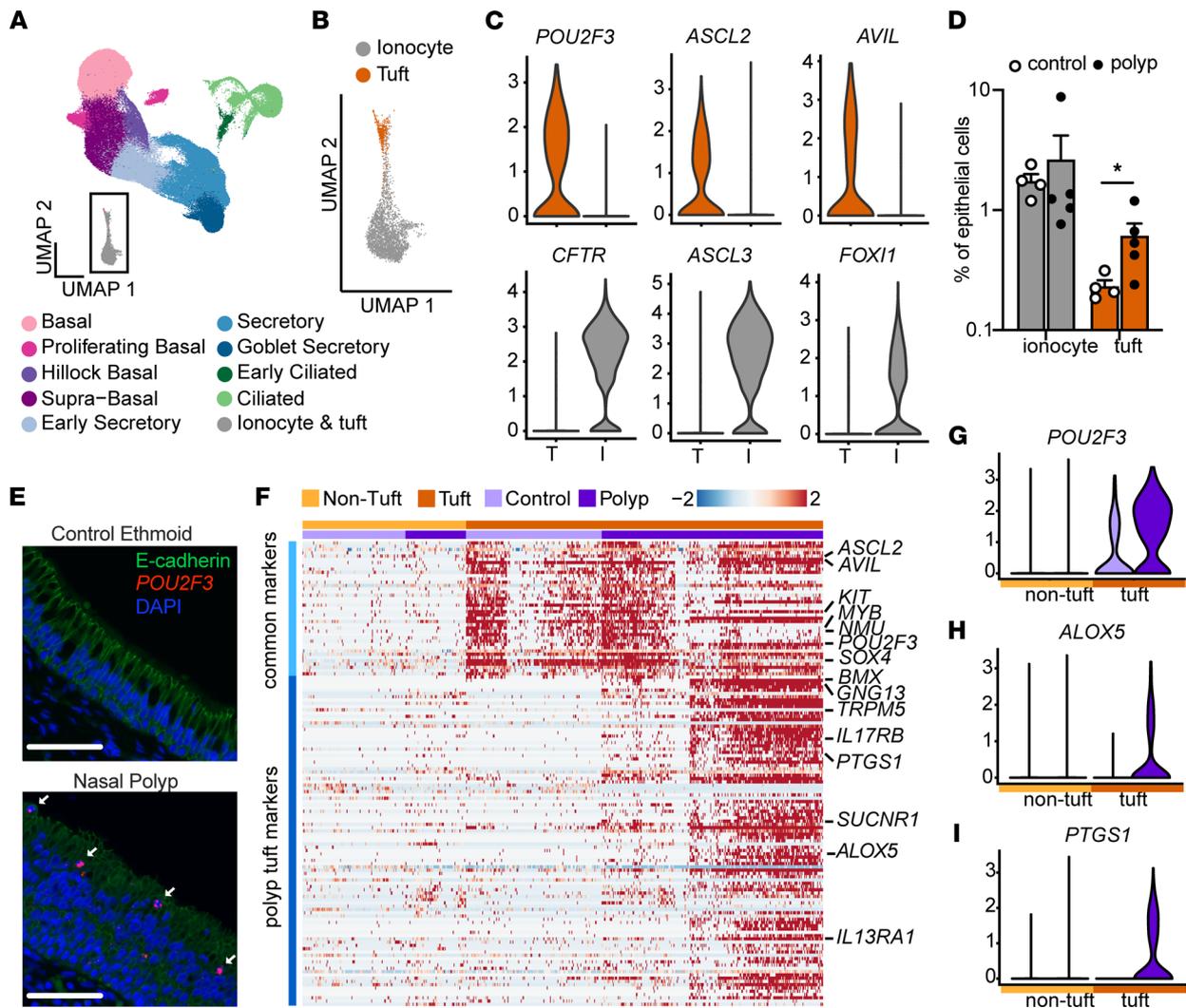
Figure 1. Single-cell sequencing reveals expansion and allergic activation of tuft cells in nasal polyps. (**A**) Uniform manifold approximation and projection (UMAP) of scRNA-Seq of epithelial cells from healthy ethmoid sinus (control; *n* = 4) or nasal polyp (*n* = 5) (total cells = 116,358) reveals 10 cell types. (**B**) Expanded view of inset in **A** showing tuft cells and ionocytes identified by hierarchical subclustering. (**C**) Expression of tuft cell and ionocyte marker genes in tuft and ionocyte subclusters. (**D**) Percentage of ionocytes and tuft cells among total epithelial cells in control or polyp. Error bars indicate mean ± SEM. *$P < 0.05$ by Mann-Whitney *t* test with correction for multiple comparisons. (**E**) RNA in situ hybridization for *POU2F3* (red) and immunofluorescence for E-cadherin (shown in green) identifies increased numbers of tuft cells (arrow) in nasal polyp epithelium as compared with control ethmoid (representative of 3 samples from 3 patients of each type). Scale bars: 60 μm. (**F**) Shared tuft cell marker genes ("common markers") and differentially expressed genes (DEGs) ("polyp tuft markers") in tuft (dark orange) and nontuft cells (light orange) from control (light purple) and polyp (dark purple) epithelium. Expression of representative (**G**) common tuft cell marker *POU2F3* and polyp tuft markers (**H**) *ALOX5* and (**I**) *PTGS1*.

We found that this T2 gene score was broadly increased across epithelial cell clusters in patients with polyps compared with controls (Supplemental Figure 3A). To build upon this finding, we sought to define the entire repertoire of pan-epithelial gene expression alterations in nasal polyps. We performed differential expression analysis of each cell type, comparing polyp with control groups. We then categorized DEGs based on the number of epithelial cell types in which they were found (Figure 2A and Supplemental Figure 3B). Most DEGs were only identified in 1–2 epithelial clusters, suggesting cell type–specific responses, but a small subset of DEGs were found in 9 or more epithelial cell types. We defined these DEGs as pan-epithelial. Among these DEGs, we identified 2 coexpressed gene sets (Supplemental Figure 3C). We determined that one set (including *CST1*, *POSTN*, *NTRK2*, and *ALOX15*) was upregulated by IL-13 (Figure 2B), consistent with prior work (4, 23), while the second set of genes (including *PTH-LH*, *SLC6A8*, *IGFBP3*, *NDRG1*, *EGLN3*, and *ERO1A*) was not IL-13 inducible (Figure 2B). We reasoned that tuft cell–derived eicosanoids might act on the epithelium to induce this gene signature based on prior reports of arachidonic acid pathway dysregulation in nasal polyposis (25) and our observation of allergic

tuft cell expansion. We stimulated human airway epithelial cells with leukotrienes and prostaglandins and found that prostaglandin E_2 (PGE_2) increased expression of the second gene set (Figure 2, C and D, and Supplemental Table 7) but not the IL-13–responsive genes.

To validate our finding of a novel PGE_2 gene expression signature in the nasal polyp epithelium, we analyzed published data from single-cell sequencing of whole polyp tissue (16). We reidentified 7 epithelial cell clusters using published markers (Figure 2E) and performed differential expression analysis for each epithelial cell type between samples derived from participants with or without polyps. The PGE_2 activation score was robustly upregulated in all the epithelial cell type clusters in this independent single-cell data set (Figure 2F and Supplemental Table 7).

IL-13 expands and programs airway tuft cells toward PGE_2 production. IL-13 is critical to goblet cell metaplasia in T2 inflammation of the airway, as well as to both tuft and goblet cell expansion in the intestine. To explore the role of IL-13 in tuft cell expansion and PGE_2 production in the airway, we induced systemic IL-13 overexpression in mice using hydrodynamic plasmid injection (Figure 3A). Injected mice had high plasma IL-13 levels, whereas circulating IL-13 was not detected in control mice (Supplemental Figure 4A). Tuft cells were increased in both the nasal (Figure 3, B and C) and tracheal epithelium (Supplemental Figure 4, B and C) following IL-13 overexpression. Single-cell sequencing revealed the emergence of 2 distinct tuft cell clusters under IL-13 stimulation (Figure 3, D and E; Supplemental Figure 4, D and E; and Supplemental Table 6). Gene expression differences between IL-13–emergent mouse nasal tuft cells versus control mouse tuft cells did not correlate with previously identified subsets of tuft cells in untreated mouse trachea or intestine (Supplemental Figure 4F). However, the emergent mouse nasal tuft cell clusters expressed genes similar to those observed in the allergic tuft cells of patients with CRSwNP, as evidenced by an increase in the mean expression of the polyp tuft marker genes (i.e., "polyp tuft score") compared with the tuft cells from unstimulated mice (Figure 3F). Because this mouse model recapitulated key aspects of the tuft cell changes observed in human CRSwNP, we then applied this model to determine if PGE_2 production in the respiratory tract was dependent on allergic tuft cells. Using tuft cell–deficient *Pou2f3*$^{-/-}$ mice exposed to systemic IL-13, we found a marked reduction in PGE_2 metabolites (PGEMs) in tracheal lysates of *Pou2f3*$^{-/-}$ compared with wild-type mice (Figure 3, G and H). PGE_2 was also markedly reduced in tracheal organoids generated from *Pou2f3*$^{-/-}$ mice, supporting an epithelial cell of origin (Figure 3, G and I).

IL-13–dependent tuft cell programming and PGE_2 activation are common features of upper and lower allergic airway disease. To expand our findings across allergic diseases of the upper and lower respiratory tract, we collected epithelial brushings from the sinus of patients with both CRSwNP and asthma, CRSsNP, and control participants (Supplemental Table 1). Consistent with our single-cell sequencing data, epithelial type 2 activation was increased in polyp brushes (Figure 4A), while it was not increased in CRSsNP. In further agreement with our scRNA-Seq data, the "polyp tuft score" was also increased in polyp but not CRSsNP participants (Figure 4B) and paralleled by an increase in the PGE_2 score (Figure 4, C and D). Consistent with our finding that IL-13–treated mice deficient in tuft cells had reduced PGE_2 in the respiratory tract, and further supporting a causal link between IL-13, allergic tuft cell generation, and PGE_2 production, we found a strong correlation between the polyp tuft score and PGE_2 activation score, as well as between the T2 inflammation and epithelial PGE_2 activation scores in these participants (Figure 4, D and E).

Since chronic IL-13 stimulation in mice led to tuft cell expansion and PGE_2 production in both the upper and lower airway, we reasoned that T2 inflammation may similarly drive tuft cell activation throughout the airway in humans. Indeed, allergic tuft cell transcripts and PGE_2 activation were increased in the bronchial epithelium of asthmatics with T2 inflammation (Figure 4, F and G).

PGE_2 regulates epithelial CFTR-dependent fluid secretion and mucociliary transport. To examine the effects of PGE_2 on respiratory epithelial function, we cultured healthy human tracheal and sinus epithelium in the presence or absence of PGE_2. Of the 4 PGE_2 receptors (EP1–4), EP4 and to a lesser extent EP2 are expressed in airway epithelial cells (26). We found that chronic exposure to PGE_2 progressively increased 3D organoid diameter in an EP4- but not EP2-dependent fashion (Figure 5, A and B), similar to effects reported in intestinal epithelium (27, 28). Increased organoid diameter in response to PGE_2 also occurred in sinus epithelium from polyp patients (Supplemental Figure 5A). Based on diameter, we estimated organoid surface area increased 1.8-fold with PGE_2 treatment, whereas cellular DNA content increased 1.4-fold (Supplemental Figure 5B), reflecting a modest augmentation in cell number and suggesting additional mechanisms of organoid expansion. Moreover, we observed that
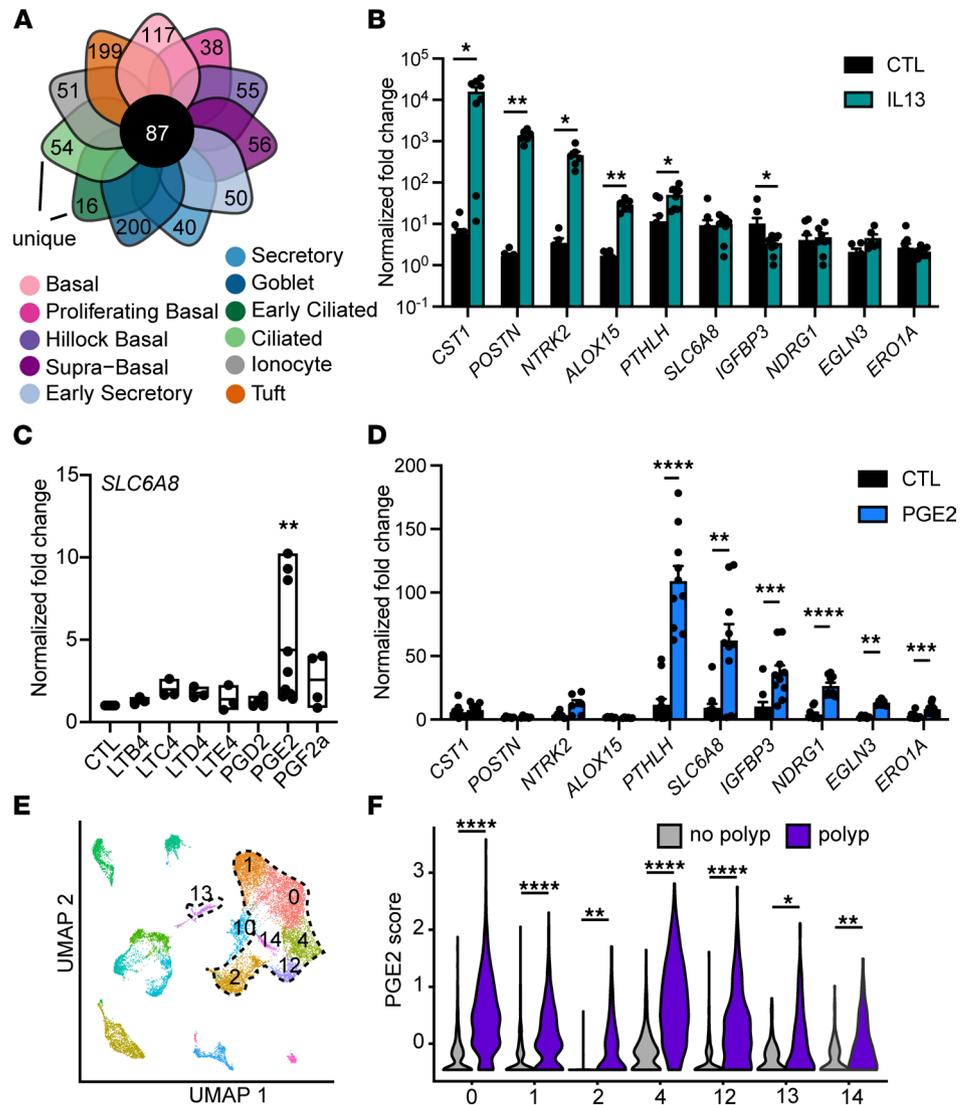
Figure 2. Pan-epithelial gene signatures in nasal polyps are imparted by IL-13 and prostaglandin E₂. (**A**) Among all DEGs for each cell type, 87 genes were upregulated in at least 9 cell types in polyp epithelium compared with controls and defined as pan-epithelial. (**B**) Fold change in normalized gene expression for tracheal epithelial cells cultured at air liquid interface (ALI) and stimulated with IL-13 ($n = 10$ wells from 6 donors, *$P < 0.05$; **$P < 0.01$ by ANOVA with Tukey correction). (**C**) Fold change in normalized *SLC6A8* gene expression in human tracheal epithelial cells cultured at ALI and stimulated with indicated eicosanoids ($n = 9$ donors, **$P < 0.01$ by ANOVA with Dunnett's correction). Represents similar responses for all genes as shown in **D**. (**D**) Fold change in normalized gene expression for tracheal epithelial cells cultured at ALI and stimulated with prostaglandin E₂ (PGE₂) ($n = 10$ wells from 6 donors, **$P < 0.01$; ***$P < 0.001$; ****$P < 0.0001$ by ANOVA with Tukey correction). (**E**) UMAP of scRNA-Seq data from surgical sinus tissue of participants with CRSwNP ("polyp") or patients with CRS without nasal polyps (CRSsNP) ("no polyp") whole polyp or nonpolyp sinus tissue (16). Epithelial clusters encircled with dashed line. (**F**) PGE₂ response gene score in polyp and nonpolyp epithelial clusters. *$P < 0.05$; **$P < 0.01$; ****$P < 0.0001$ by linear mixed model. Statistical calculations relating to this figure are included in Supplemental Table 7. For **B** and **D**, data shown as mean ± SEM. For **C**, horizontal line shows mean with bars indicating range.

acute PGE₂ application caused organoid swelling over minutes to hours, which was blocked by inhibition of the CFTR (Figure 5C), suggesting organoid swelling was caused by ion and fluid movement. Indeed, PGE₂ activated CFTR-dependent currents in 2D cultured human upper airway epithelial cells (Figure 5D). Effective mucociliary transport (MCT) is highly dependent on epithelial ion and fluid secretion, as exemplified by the pathology observed in the disease cystic fibrosis. Consistent with this, we found that PGE₂ stimulation increased MCT on the surface of cultured human airway epithelial cells in a CFTR-dependent fashion (Figure 5E).
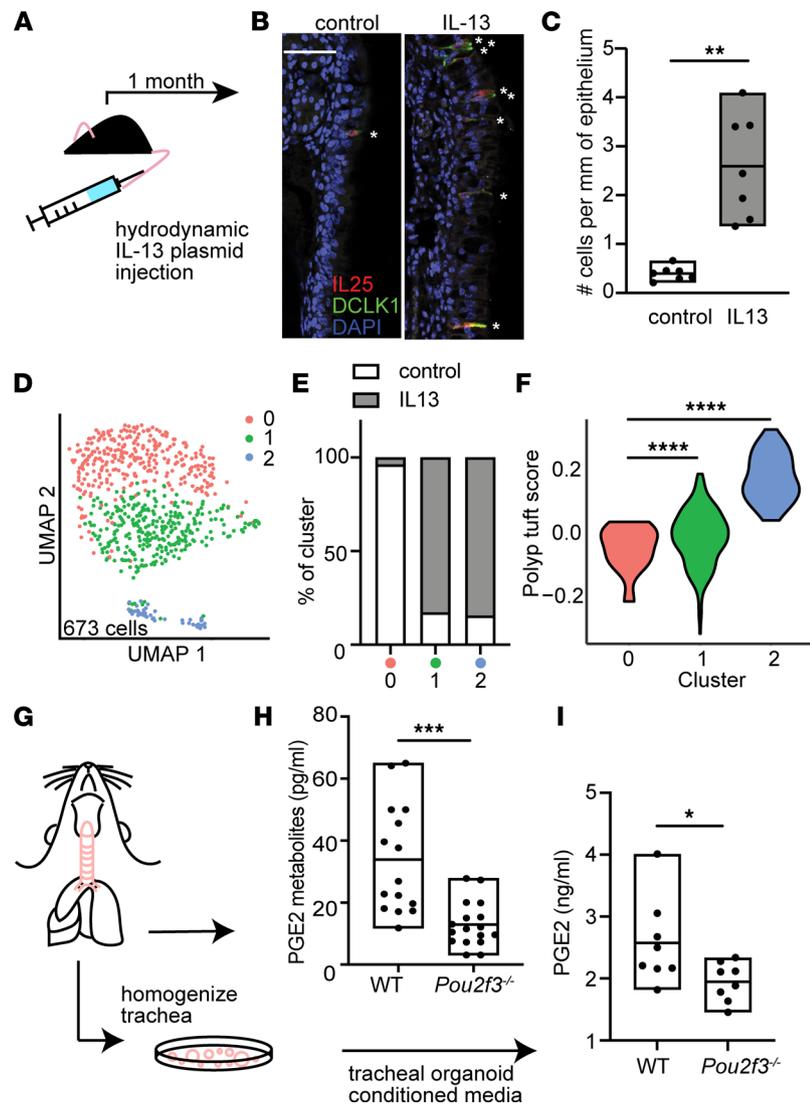
Figure 3. IL-13 expands and programs airway tuft cells toward PGE$_2$ production. (A) T2 inflammatory mouse model system. **(B)** Representative sections of mouse nasal epithelium after 1 month of IL-13 overexpression or IgG control. Stars mark dual staining IL-25$^+$ and DCLK1$^+$ tuft cells. Bar indicates 50 μm. **(C)** Quantification of tuft cells in nasal epithelium in control and systemic IL-13 expression. **$P < 0.01$ by t test. **(D)** Subclustering of tuft cells from control or IL-13–overexpressing mouse nasal epithelium. **(E)** Percentage of tuft cells derived from control or systemic IL-13 conditions in each subcluster in **D**. **(F)** Human polyp allergic tuft cell gene score in mouse nasal epithelial tuft cell subclusters. ****$P < 0.0001$ by linear regression model. **(G)** Schematic of protocol to measure **(H)** PGE$_2$ metabolites (PGEMs) in whole tracheal tissue from WT or *Pou2f3$^{-/-}$* mice exposed to systemic IL-13 or **(I)** PGE$_2$ in media from tracheal organoids derived from WT or *Pou2f3$^{-/-}$* mice. **(H** and **I)** *$P < 0.05$; ***$P < 0.001$ by t test. For **C**, **H**, and **I**, line is at mean and bars indicate max/min (range).

Discussion

Though they were first observed throughout the conducting airways more than 50 years ago, the rarity of airway tuft cells has been a challenge to their study. As a result, the phenotype and function of these cells has been elusive, and conceptual models have relied heavily on studies in the mouse small intestine. Here we show that tuft cells in the context of allergic diseases of the respiratory tract expanded in number and adopted a transcriptional program that augmented PGE$_2$ production throughout the airways. PGE$_2$ signaling, in turn, promoted epithelial fluid secretion and MCT via activation of the CFTR channel. Together, these findings suggest that tuft cells direct mucociliary homeostasis in the allergic airway and provide insight into their critical homeostatic function.

The foremost purpose of the conducting airways is to defend against particles, microbes, and chemicals while transmitting air to the lung for gas exchange. Mucociliary clearance is the primary airway
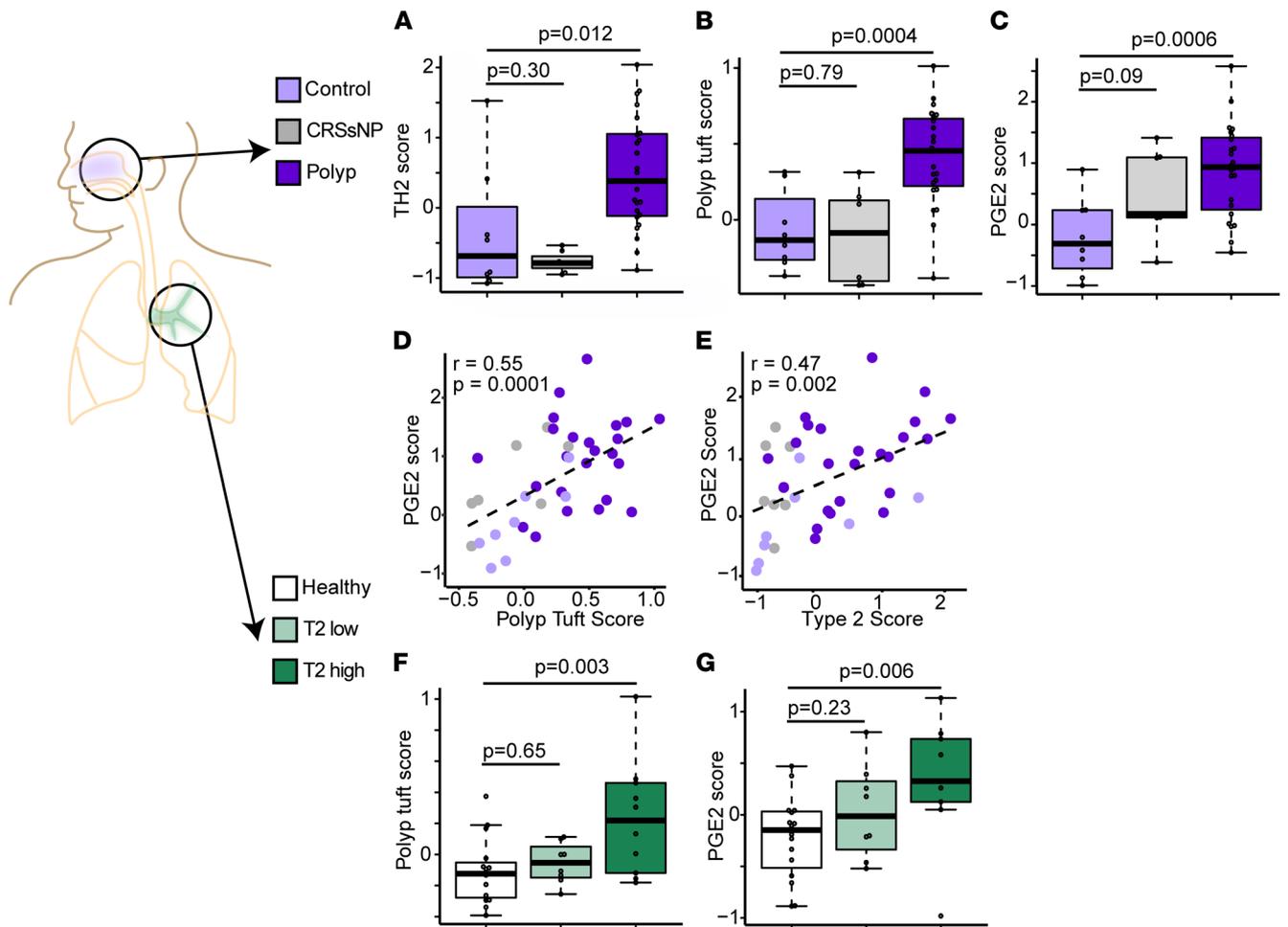
Figure 4. Tuft cell and PGE$_2$ activation are common features of upper and lower allergic airway disease. (**A**) T2 (3 gene) score, (**B**) polyp tuft score, and (**C**) PGE$_2$ score in RNA-sequenced bulk epithelial brushings from sinus tissue of control patients (light purple) or patients with CRS without asthma or nasal polyps ("CRSsNP"; gray) or CRS with asthma and nasal polyps ("Polyp," dark purple). (**D**) Correlation between PGE$_2$ score and polyp tuft cell score in sinus. (**E**) Correlation between PGE$_2$ score and T2 score in sinus. (**A–E**) n = 8 control, n = 7 CRSsNP, n = 24 polyp participants, as in Supplemental Table 1. (**F**) Polyp tuft score and (**G**) PGE$_2$ score in RNA sequencing of bulk epithelial brushings of the bronchus of healthy participants or asthmatic participants classified as either T2 low or T2 high. (**F** and **G**) n = 16 healthy, n = 8 T2 low, n = 11 T2 high. For **A–C**, **F**, and **G**, bars represent 25th–75th percentiles with line at median, error bars indicating range, and whiskers extending from largest value (upper whisker) no farther than 1.5 × IQR from the hinge (where IQR is the distance between the first and third quartiles) to smallest value no farther than 1.5 × IQR (lower whisker).

defense and therefore critical to its proper function. An abundant body of literature has shown that ionic and fluid movement across the epithelium is critically important in maintaining the function of the airway mucous barrier, impacting the biophysical properties of gel-forming mucins, optimizing the activity of antimicrobial peptides, and enabling mucociliary transit (29–31). These nonredundant roles are exemplified by the consequences of genetic CFTR dysfunction and cystic fibrosis. In the allergic airway, the composition and functional properties of the mucus layer are substantially altered by IL-13, which promotes transcriptional pathways leading to goblet cell expansion, shifts in the production of gel-forming mucins from MUC5B to the more pathologic MUC5AC (32), and alterations in antimicrobial peptides and ion transporters (4), resulting in the airflow obstruction and airway mucus plugging that are prominent features of T2-high asthma (33). In the context of these dramatic changes in mucus quantity and quality, the expansion and programming of tuft cells that enable production of PGE$_2$ may serve to hydrate the mucus and promote clearance via CFTR. The specific importance of CFTR activity in maintaining fluid transport in the allergic airway is reinforced by the observation that CFTR gene mutations are found in patients with asthma or nasal polyps (without cystic fibrosis) at higher rates than in healthy control populations (34). While PGE$_2$-enhanced mucus transport may be beneficial in the context of pathologic mucus production in the allergic airway, further studies are needed to define
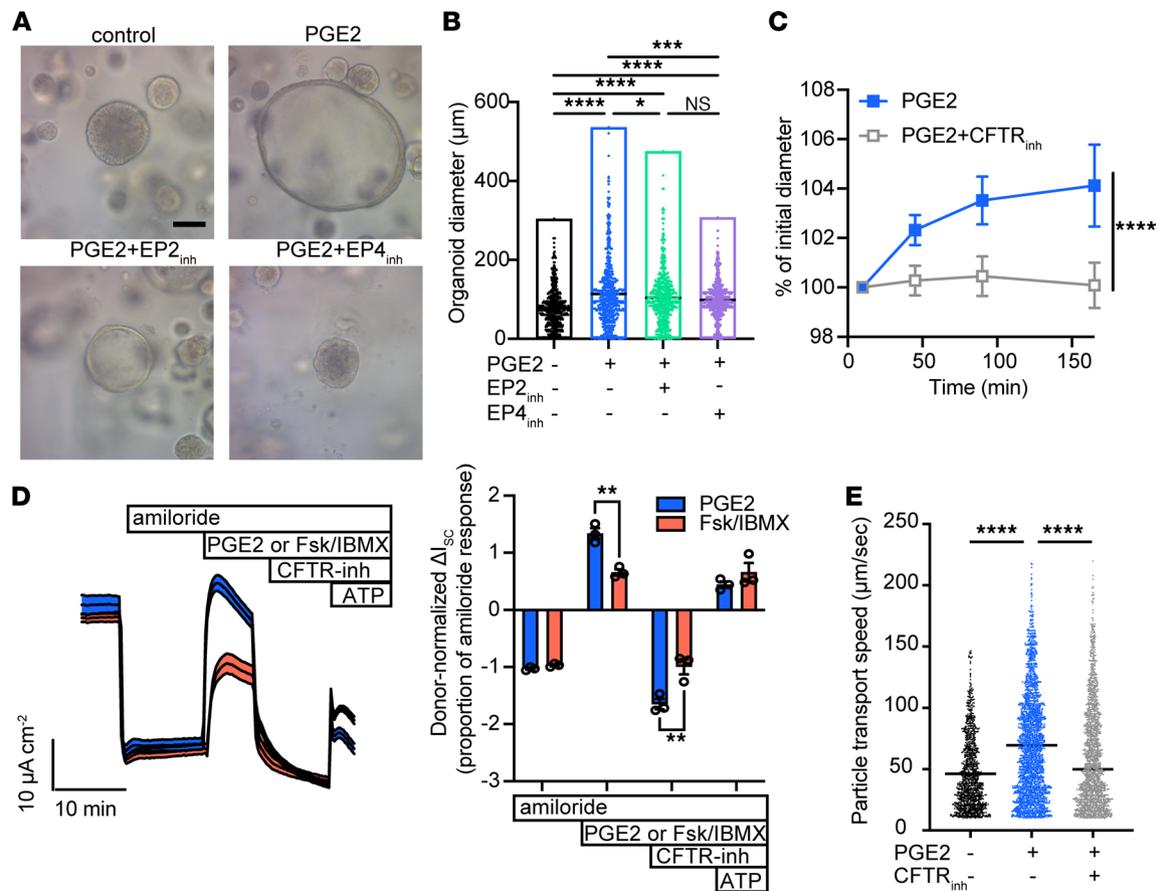
Figure 5. PGE$_2$ regulates epithelial CFTR-dependent fluid secretion and mucociliary transport. (A) Human tracheal epithelial organoids cultured for 21 days in the absence or presence of daily stimulation with 1 μg/mL PGE$_2$, or with PGE$_2$ + EP2 inhibitor (EP2$_{inh}$) or PGE$_2$ + EP4 inhibitor (EP4$_{inh}$). Original magnification, 20×; scale bar, 100 μm. representative of at least 2–3 wells per experiment in at least 4 independent experiments with different tracheal and sinus epithelial donors. **(B)** Diameter of organoids in **A**. Each dot represents 1 of 200 randomly selected organoids per well × 3 replicate wells per condition. Line indicates median diameter. ****$P < 0.0001$, ***$P < 0.001$, *$P < 0.05$, by 1-way ANOVA with Holm-Šídák correction. **(C)** Diameter of chronically PGE$_2$-treated organoids as in **A** and **B** immediately after acute stimulation with PGE$_2$ ± CFTR inhibitor 172 (CFTR$_{inh}$). Value ± 95% CI at each time point represents 20 serially imaged organoids per condition. Representative of 2 independent experiments. ****$P < 0.0001$ by 2-way ANOVA. **(D)** Short-circuit current measured in human nasal epithelial cells at ALI after inhibition of epithelial sodium channel–dependent current with amiloride, followed by treatment with PGE$_2$ or cAMP activation by forskolin/IBMX, then by CFTR inhibition, and finally by ATP-dependent activation. Donor-normalized quantification of short-circuit currents shown in right panel, with each dot representing treatment of an individual epithelial donor. **$P < 0.01$ by 2-way ANOVA. **(E)** Particle transport speed on the surface of tracheal epithelial cells cultured at ALI and stimulated with PGE$_2$ ± CFTR inhibitor 172. Each dot represents 1 tracked particle on the surface of at least 3 replicate wells from each of 3 donors per condition. ****$P < 0.0001$ by 2-way ANOVA of log-transformed speeds. Line indicates mean.

the full spectrum of PGE$_2$ effects, as well as the function of other secreted factors derived from tuft cells. Nevertheless, our study firmly establishes the IL-13–programmed tuft cell as part of the epithelial remodeling that occurs in the allergic airway.

Although tuft cells display high expression of *PTGS1* (1 of 2 enzymes that catalyze the rate-limiting step in prostaglandin production), other cell types also produce PGE$_2$. Some, such as mast cells, are concurrently elevated in nasal polyposis, allergic rhinitis, and asthma (35–37). Our data show reduced PGE$_2$ metabolites in epithelial organoids as well as whole tracheal tissue from tuft cell–deficient mice, suggesting that tuft cells are themselves a source of this molecule in airway epithelium. It is not clear how tuft cell–dependent PGE$_2$ production differs qualitatively or quantitatively from that of other PGE$_2$-producing cells. One possibility is that tuft cell–derived PGE$_2$ acts predominantly on neighboring epithelial cells, while immune cell–derived PGE$_2$ production may be more critical in the submucosa. Further, while our epithelial organoids strongly suggest tuft cells are themselves a source of PGE$_2$, it is also possible that tuft cell–derived signals stimulate PGE$_2$ production from other sources.

Although PGE$_2$ is known to be dysregulated in the T2 inflammatory environment, its effects on cells and tissues have proved to be complex and pleomorphic. For instance, it can promote vasodilation and

tissue edema through direct smooth muscle relaxation (38), has antiinflammatory effects on both the innate and adaptive immune system (39), can promote stem cell survival and tissue regeneration (40), and has well-described functions in gastrointestinal mucosal protection, secretion, and motility (41). These functional consequences are context dependent. Although our work focuses on the epithelium, tuft cell–dependent PGE_2 production likely has broad effects on diverse cell types in the respiratory tract.

Our finding that PGE_2 activated CFTR-dependent epithelial ion channels in the respiratory epithelium to induce fluid secretion is consistent with a large body of literature showing similar action in the intestinal epithelium (27). Although our study has focused on the role of PGE_2 in epithelial ion transport and mucociliary function, it is notable that both the sinus and intestinal epithelium are susceptible to polypoid epithelial growth. In the intestine, polyp formation is dependent on local PGE_2 production and can be blocked experimentally and clinically by inhibition of cyclooxygenase 1 or 2 (COX-1 or -2) (42, 43). Blockade of EP4 also abrogates intestinal polyp formation (44). Further, a number of the genes we found to be PGE_2 responsive are linked to cell growth and differentiation and are dysregulated in some cancers (45–47), while a growing body of work has implicated tuft cells in cancer formation or progression (48–51). Despite these similarities, intestinal polyps are precancerous while nasal polyps are stably benign. Nevertheless, in the context of this broad literature, one may hypothesize that tuft cell–derived products such as PGE_2 could influence neoplastic growth, including nasal polyp formation, in a genetically susceptible host. Further study of the potentially pleiotropic impacts of tuft cell–dependent PGE_2 production in the airway is needed.

The treatment paradigm for nasal polyposis, previously managed with surgery and topical corticosteroids, has been revolutionized by inhibition of IL-4 and IL-13. Yet the therapeutic effect of type 2 cytokine blockade is incomplete (52), suggesting additional pathologic mechanisms. Our data reveal an elevated PGE_2 score in CRSwNP, raising the question of whether targeting this pathway may be of clinical benefit. While the patient group in this study was too small to correlate transcriptional signatures of T2 inflammation, tuft cell activation, and PGE_2 stimulation with clinical measures or disease endotypes, such correlations in larger patient cohorts will inform the use of these biomarker signatures for therapeutic discovery.

COX inhibitors have enjoyed success in the clinical management of intestinal polyposis, but such drugs prove problematic when deployed in nasal polyposis where a significant subpopulation display aspirin sensitivity (or aspirin-exacerbated respiratory disease, AERD), characterized by wheezing and hives. The mechanism of this sensitivity to COX inhibition is thought to be due to shunting of arachidonic acid toward leukotrienes (LTs) and reduced smooth muscle EP2 receptor activity leading to bronchoconstriction and inflammation (53). Reduced EP2 expression in patients with AERD compared with aspirin-insensitive CRSwNP may further contribute to the relative imbalance of LT versus PGE_2 effects on inflammation and bronchoconstriction (54). While the relative deficiency of PGE_2 and excess LT mediated by COX inhibition is pathologic in patients with AERD, pharmacologic manipulation of specific prostaglandin receptor subtypes could prove beneficial in CRS.

In sum, this work identifies a transcriptional shift in tuft cells in human airway disease that alters their signaling potential. It reveals a critical role for tuft cells in modulating epithelial homeostasis within the landscape of the respiratory tract and deepens our understanding of how epithelial functions are coordinately altered under allergic conditions.

Methods

Sinus study participants

Participants between the ages of 18 and 75 years were recruited from the UCSF Otolaryngology clinic between 2013 and 2019 (Supplemental Table 1) to participate in a UCSF Sinus Tissue Bank. The UCSF Committee on Human Research approved the study, and all participants provided written informed consent. Cytologic brushes were collected from nasal polyps or ethmoid sinus at the time of elective endoscopic sinus surgery from patients with physician-diagnosed chronic rhinosinusitis with or without nasal polyps on the basis of established guidelines. Participants with cystic fibrosis were excluded from the study. Non-CRS control participants were those who were undergoing endoscopic sinus surgery for alternative indications (i.e., septal deviation, pituitary surgery, and so on).

Human biospecimen collection

Cytologic brushes obtained from the ethmoid sinus or nasal polyps were placed in RNAlater (Qiagen) for RNA extraction for bulk RNA sequencing or into 10% FBS in RPMI (Gibco) on ice for scRNA-Seq analysis or in vitro culture.

Preparation of human biospecimens for scRNA-Seq

Brushes in 10% FBS/RPMI were vortexed on low speed for 2 minutes, brushes were removed, and media were centrifuged at 300g for 10 minutes at 4°C. Cell pellets were resuspended in 0.25% trypsin and placed on an Eppendorf ThermoMixer C at 37°C at 300 rpm for 15 minutes. Trypsin was neutralized with complete media, and cells were pelleted and then resuspended in 1× Pharm Lyse (BD) for 10 minutes followed by neutralization in complete media. Cells were pelleted at 300g for 10 minutes and resuspended in 0.4% BSA in PBS prior to passing through a 40 μm cell strainer (Falcon, Corning). A total of 40,000 cells were loaded onto the 10x Genomics Single Cell 3′ v3 chip.

Single-cell RNA-Seq computational pipeline and analysis for human biospecimens

The 10x Genomics Single Cell 3′ v3 chemistry was employed. Initial pre-processing of the 9 participants' 10x Genomics scRNA-Seq data, including demultiplexing, alignment to the hg38 human genome, and unique molecular identifier–based (UMI-based) gene expression quantification, was performed using Cell Ranger (version 3.0, 10x Genomics).

Preliminary quality control

Data were collected on 183,167 cells from 9 samples. We filtered out low-quality cells with fewer than 200 genes detected or with greater than 75% of mapped reads originating from the mitochondrial genome. We additionally safeguarded against doublets by removing cells with a UMI count greater than the 98th percentile of UMI counts for each sample. Prior to downstream analysis, select mitochondrial and ribosomal genes (genes beginning with MT-, MRPL, MRPS, RPL, or RPS) were removed. The preliminary quality-controlled data set consisted of 176,803 cells and 23,778 genes.

To account for differences in coverage across cells, we normalized and variance stabilized UMI counts using the SCTransform method in the Seurat R package (55, 56). In addition to adjusting for sequencing depth, we also adjusted for the proportion of mitochondrial reads.

Preliminary analyses to identify epithelial cells

Data integration, dimensionality reduction, and clustering. Data from the 9 participants were combined using single-cell integration implemented in Seurat v3. Integration was carried out using the top 30 dimensions from a canonical correlation analysis based on SCTransform-normalized expression of the top 3000 most informative genes, defined by gene dispersion using the Seurat's SelectIntegrationFeatures function. Integrated data were then clustered and visualized using the top 20 principal components. For visualization, we reduced variation to 2 dimensions using UMAP (n.neighbors = 50, min. dist = 0.3) (57). Unsupervised clustering was performed by using a shared nearest neighbor graph based on 20 nearest neighbors and then by determining the number and composition of clusters using a smart local moving algorithm (resolution = 0.4). This algorithm identified 20 preliminary clusters.

Cluster markers. To identify cluster markers, we carried out pairwise differential expression analysis comparing log-normalized expression in each cluster to all others using a Wilcoxon rank sum test. Markers were identified as genes exhibiting significant upregulation when compared against all other clusters, defined by having a Bonferroni-adjusted $P < 0.05$, a log fold change > 0.25, and >10% of cells with detectable expression. This analysis was then performed separately for each participant using Seurat's FindConservedMarkers function to determine if marker genes were consistent across participants. Cluster markers were required to have significant upregulation in at least half of the participants.

Several clusters (clusters 11–13, 18, 19) had markers associated with both epithelial and immune cell types. These cells were subclustered using the same methods described above to separate immune and epithelial cells. Subclustering resulted in 8 epithelial and 7 immune subclusters. The data set was divided into immune (8153 cells) and epithelial (168,650 cells) data sets. Dimensionality reduction and clustering were performed separately for each data set, resulting in 10 immune and 22 epithelial clusters.

Additional quality control and doublet detection. Potential doublets were assessed using the doubletCluster function in the scran R package (58, 59), which can be used to identify clusters of doublets, and the scds R package (60), which assigns a doublet score to each cell. Epithelial clusters 18, 20, and 21 were identified as likely doublet clusters and were removed from further analysis. In addition, cells with high binary classification-based doublet scores (BCDS > 0.5) were also excluded from further analysis. Epithelial cluster 3 was composed of cells with a high percentage of mitochondrial reads. Therefore, cluster 3 and all other cells with > 40% mitochondrial reads were excluded. Epithelial cluster 14 had only 3 consistent markers across participants, including hemoglobin HBA1, HBA2, and HBB. These cells were also excluded from further analysis.

Final epithelial data set

The final quality-controlled epithelial data set included 116,358 cells and 23,778 genes observed in at least 1 cell. Final data integration, dimensionality reduction, clustering, and marker finding were performed, as described above. We identified 15 clusters, which were collapsed into 10 cell types based on the expression of known marker genes (Supplemental Tables 2 and 3).

Subclustering of rare epithelial cells. Epithelial cluster 10 appeared to be a combination of rare cell types, including both ionocytes and tuft cells. We hierarchically clustered these cells based on scaled normalized expression of previously published cell type markers (19, 21, 22). Euclidean distance was used to measure similarity between cells, and cells were clustered using the complete linkage method in the hclust function in R.

Ionocyte and tuft cell markers were identified as described above. In addition, tuft cell markers were generated separately for control and polyp cells to understand heterogeneity in gene expression between polyp and control tuft cells. Tuft cell markers were categorized as "common" if they were significant markers in both control and polyp cells, "polyp specific" if they were significant in polyp cells only, and "control specific" if they were significant in control cells only.

Pseudo-bulk differential expression. To identify DEGs between control and polyp samples while accounting for clustering of cells within participants, we performed pseudo-bulk differential expression analysis separately for each cell type (61–63). Within each cell type, expression counts were summed across all cells for a participant, resulting in a single expression measurement for each gene for each participant. Pseudo-bulk expression was compared between participants with polyps and controls using bulk RNA-Seq analysis methods with the edgeR R package (64, 65). Genes with Benjamini-Hochberg (66) adjusted *P* values less than 0.05 were considered differentially expressed.

Hierarchical clustering of pan-epithelial genes. DEGs were classified as pan-epithelial if they were upregulated in polyp versus control in 9 or more of the 11 cell types. These genes were hierarchically clustered based on euclidean distance using the complete linkage method to identify modules of related genes.

Gene signature scores and comparisons. Gene set signature scores were calculated for each cell by taking the average of scaled log-normalized expression of the genes in the signature set. We calculated the following gene signature scores: type 2 (3 gene) score (23), PGE_2 score, common tuft marker score, polyp tuft marker score, Haber tuft 1 and tuft 2 scores (22), and Montoro tuft 1 and tuft 2 scores (6). Full lists of genes for each signature are available in Supplemental Table 5 or in listed references. Linear mixed models were used to compare gene signature scores between groups with the lmerTest R package (67, 68). Models included a participant-specific random intercept to account for clustering of cells within participants. Tuft cell signatures from tuft or nontuft cells from controls or polyps were also compared to published human tracheal tuft cells (19) or consensus mouse tuft cell markers (21).

Comparison to published data sets

To confirm our scRNA-Seq findings, we reanalyzed data from Ordovas-Montanes et al. (16). Quality control and filtering of cells was performed as described (16). Data integration, dimensionality reduction, clustering, marker finding, and calculation and modeling of the PGE_2 score were performed as described above. We identified 17 clusters, 7 of which included epithelial cells based on comparison to markers published in the original analysis. Gene scoring was performed as above. Statistical comparisons are included in Supplemental Table 7.

For analysis of bronchial epithelial brushes, we analyzed data from National Center for Biotechnology Information's Gene Expression Omnibus (NCBI GEO) under the accession number GSE109484. Normalized expression values were centered and scaled before calculation of gene signature (scores are described in *Gene signature scores and comparisons*). Signature scores were compared between groups using 1-way ANOVA.

Gene set enrichment analysis

Gene set enrichment analysis was performed using the EnrichR R package with the GO Biological Process 2018 database.

RNA extraction

Cytology brushes frozen in RNAlater were defrosted on ice and diluted with sterile 1× PBS. Samples were centrifuged at 18,000g for 20 minutes, and brushes were removed and placed into a Lyse E tube. Pellets were resuspended in RLT/β-mercaptoethanol and added to the Lyse E tube. Samples were agitated in a bead beater (MP Biomedicals FastPrep-24 Classic) for 30 seconds. Samples were centrifuged at 500g for 1 minute and transferred to an Allprep (Qiagen) spin column. RNA and DNA were prepared according to the manufacturer's instructions. Residual DNA was removed from the purified RNA by incubation with RNase-Free DNase (Promega) for 30 minutes at 37°C. DNase was removed from the preparation via a second RNA cleanup using the Qiagen RNeasy Kit. RNA concentration was determined using NanoDrop (Thermo Fisher Scientific), and RNA quality was assessed using Agilent Pico RNA kit.

For cultured cells, ALI Transwell inserts or organoids were lysed in RLT plus buffer (Qiagen) and RNA purified using the Qiagen RNeasy Kit according to the manufacturer's instructions. Equal quantities of RNA were reverse-transcribed using the SuperScript VILO cDNA synthesis kit (Thermo Fisher Scientific) and amplified using Power SYBR Green PCR master mix (Thermo Fisher Scientific) using the primers listed in Supplemental Table 4.

Bulk RNA-Seq for human biospecimens

For whole-transcriptome sequencing, we first used the Ion AmpliSeq Transcriptome Human Gene Expression Kit (catalog A26325, Life Technologies) to enable gene-level expression analysis from small amounts of RNA. We generated barcoded sequencing libraries per the manufacturer's protocol from 10 ng of RNA isolated from the 24 stimulation samples detailed above (12 pairs). Libraries were sequenced using the Ion PI template OT2 200 kit v3 for templating and the Ion PI sequencing 200 kit v3 kit for sequencing. Barcoding allowed all 24 samples to be loaded onto 3 PI sequencing chips and sequenced with an Ion Proton Sequencer using standard protocols. Read mapping was performed with the TMAP algorithm on the Proton server, and read count tables for each gene amplicon were generated using the Proton AmpliSeq plugin. Read counts for gene amplicons across all 3 runs were merged to generate the final raw expression data.

Bulk gene signature scores and comparisons

Expression data were normalized using the variance stabilizing transformation (VST) in the DESeq2 R package (69). Gene set signature scores were calculated for each sample by taking the average of scaled VST-normalized expression of the genes in the signature set (Supplemental Table 5). Linear regression models were used to compare gene signature scores between groups.

Human respiratory epithelial cell culture

Human tracheal epithelial cells were harvested from deceased organ donors according to established protocols (70). Human sinus epithelial cells were harvested from research participants undergoing endoscopic surgery using a cytobrush as described above. For Ussing chamber measurements, the inferior turbinate of healthy individuals was sampled using a protocol approved by the National Jewish Health Institutional Review Board (HS-2832), and all donors provided written informed consent prior to the procedure. Tracheal, sinus, or nasal epithelial cells were seeded onto mitomycin-treated MRC5 or irradiated NIH 3T3 fibroblast feeder layers (both from ATCC) and cultured in cultured in conditional reprogramming culture medium (71) supplemented with the ROCK inhibitor Y-27632 (ApexBIO). Expanded cells were plated on collagen-coated Transwell inserts (Corning) cultured with Pneumacult ALI (StemCell Technologies) for 21–28 days according to the manufacturer's instructions.

For organoid culture, expanded basal cells were plated in matrix (80% Matrigel, 20% media) in Pneumacult Airway Organoid Media (StemCell Technologies) according to manufacturer's instructions for 21–24 days. Cells were stimulated with PGE$_2$ (Sigma, 1 μg/mL) daily, EP2 inhibitor (PF-04418948, Cayman Chemical, 10 μM), EP4 inhibitor (L-161,982, Cayman Chemical, 10 μM), or CFTR inhibitor 172 (Sigma, 10 μM).

Ussing chamber

Electrophysiologic analyses were performed in an Ussing chamber (Physiologic Instruments). Epithelia on Transwell inserts were mounted in an Ussing chamber and bathed in a modified Ringer's solution (120 mM NaCl, 10 mM D-glucose, 3.3 mM KH_2PO_4, 0.83 mM K_2HPO_4, 1.2 mM $MgCl_2$, 1.2 mM $CaCl_2$, 25 mM $NaHCO_3$, pH 7.4), maintained at 37°C and gassed with 5% CO_2/95% O_2. Epithelia were analyzed under short-circuit conditions with intermittent pulsing (200 ms pulses at ±5 mV). Cultures were treated acutely in the Ussing chamber with subsequent additions of apical amiloride (100 μM, Alfa Aesar), apical and basolateral forskolin (20 μM, Tocris) and IBMX (100 μM, Sigma) (F/I), apical CFTR(inh)-172 (10 μM, CFTR Chemical Compound Distribution Program), and apical ATP (100 μM, Sigma). Inhibition of epithelial sodium channel–dependent current with amiloride enabled normalization of basal currents between epithelial donors.

Mice

All experimental procedures on mice were approved by the UCSF Institutional Animal Care and Use Committee. IL-25 reporter (IL25^{F25}) (10) (generated and maintained in the Locksley Lab) and *Pou2f3*$^{-/-}$ (72) (originally obtained from Mark Anderson at UCSF but maintained in the Locksley Lab since then for at least 10 generations) mice on a B6 background have been described. For single-cell sequencing, male C57BL/6J mice were obtained from Jackson Laboratories (stock 000664) at 9 weeks of age and maintained under specific pathogen–free conditions with 12-hour light/12-hour dark cycle and ad libitum access to food and water. Following 1 week of acclimation to our facility, mice were rapidly injected by tail vein injection with 2 μg of pLive in vivo expression vector (Mirus Bio) into which the mouse IL-13 coding sequence was subcloned, in a volume of sterile PBS equivalent to 10% of body weight, as described (72). Control mice received an injection of IgG1 expression vector. Overexpression of IL-13 was verified by measurement of serum IL-13 using a mouse IL-13 enhanced sensitivity flex set (BD), analyzed on an LSR Fortessa flow cytometer (BD) with FCAP Array software (BD) 1 week later, or at the time of sacrifice. For PGE$_2$ measurements or organoid culture, the protocol was as described, except that *Pou2f3*$^{-/-}$ or WT mice were bred at UCSF, and age- and sex-matched males and females between 6 and 10 weeks of age were used.

Mouse nasal epithelial preparation for single-cell sequencing

At 4 weeks after initial plasmid injection, 3 IL-13–overexpressing mice and 4 controls were sacrificed, and the nasal epithelium was dissected. Tissue was minced with scissors and epithelium separated to single-cell suspension by incubation in HBSS containing 5 mg/mL Dispase II (Gibco) for 45 minutes at room temperature, followed by 15 minutes in HBSS containing 25 μg/mL DNAse I (Roche) and filtration through a 70 μm strainer (Falcon, Corning). Following lysis of red blood cells, cells were stained for CD45 (clone 30-F11, BioLegend catalog 103108) and EpCAM (clone G8.8, BioLegend catalog 118233) antibodies for 30 minutes on ice, followed by staining with 4′,6-diamidino-2-phenylindole (DAPI) to identify dead cells. Live CD45$^-$ cells were sorted into RPMI medium on a MoFlo sorter, pooled in equal proportion from like mouse samples, then resuspended in 0.4% BSA in PBS before submission of 30,000 cells per sample for sequencing. A small aliquot of cell suspension was reserved for analysis on an LSR Fortessa flow cytometer and demonstrated more than 90% viability (by DAPI exclusion) and absence of CD45$^+$ cells.

Single-cell RNA-Seq computational pipeline and analysis for mice

Single-cell libraries from 30,000 cells per sample were prepared with the Chromium Single Cell 3′ GEM, Library & Gel Bead Kit v3 (10x Genomics PN-1000075) following the manufacturer's protocol. The libraries were sequenced on the NovaSeq 6000 (Illumina) at the UCSF Institute for Human Genetics. Initial pre-processing, including demultiplexing, alignment to the mouse genome, and UMI-based gene expression quantification, was performed using Cell Ranger (version 3.0, 10x Genomics).

Data from pooled samples from 3–4 mice per treatment group, FACS sorted to deplete immune cells (as described above), were integrated before filtering out low-quality cells according to the following parameters: min.cell = 3, min.features = 200; nFeature_RNA ≥ 300; nFeature_RNA < 5000; nCount_RNA < 20,000; percentage mitochondrial reads < 15. We used 14,172 filtered cells for analysis. We normalized and variance stabilized UMI counts using the SCTransform method in the Seurat R package (55, 56), adjusting for the proportion of mitochondrial reads. Cluster markers were manually compared to published consensus tuft cell gene expression (21) to identify a single cluster of tuft cells. We subset only this cluster and reran dimensionality reduction and clustering using SCTransform, then removed contaminating nontuft

cells before the final subclustering. Diffuse expression of canonical markers including *Pou2f3*, *Avil*, *Trpm5*, and *IL17rb* and absent expression of other nontuft lineage-defining markers confirmed the purity of the final Seurat object. We merged resulting clusters of tuft cells and then further subset and reran dimensionality reduction and clustering on the tuft cells alone. Marker lists are provided in Supplemental Table 6. Linear regression models were used to compare the polyp tuft score between tuft cell subsets.

Mouse tracheal epithelial organoid culture

Organoid growth media was composed of DMEM-F12 (Gibco) supplemented with 10 mM HEPES (Gibco), 1× Glutamax (Gibco), 100 U/mL penicillin-streptomycin, 1 mM N-acetylcysteine (Sigma), 1× N2 and B27 supplements (Gibco), 0.5 μg/mL mouse R-spondin 1 (PeproTech), 100 ng/mL mouse Noggin (PeproTech), 20 ng/mL mouse epidermal growth factor, 25 ng/mL FGF2 (PeproTech), 100 ng/mL mouse FGF10 (PeproTech), and 10 μM Y-27632 (Cayman Chemical).

Mouse tracheas of indicated genotypes were removed, cleaned, and filleted before digestion at 37°C in HBSS containing 5 mg/mL dispase II (Sigma). After vigorous vortexing, the cells and partially digested tracheal tissue were pelleted by centrifugation at 50g for 5 minutes at 4°C and then incubated for an additional 15 minutes with HBSS containing 25 μg/mL DNase I (Roche). After additional vortexing, cells and remaining tissue were filtered through a 40 μm mesh, then pelleted, and contaminating red blood cells were lysed using Pharm Lyse buffer (BD). Cells were resuspended in organoid growth media with the addition of 10% FBS, 2.5 μg/mL amphotericin B (Gibco), 100 U/mL nystatin, and 50 μg/mL gentamicin on 10 mm dishes coated with rat tail collagen (Sigma). Confluent cells were lifted with 0.25% trypsin for 30 minutes before seeding into 50 μL of matrix (80% Matrigel, 20% media). Media were collected on day 8 of culture, centrifuged at 300g for 10 minutes to remove cellular material and debris, and stored at –80°C. Aliquots were analyzed on Prostaglandin E$_2$ Parameter Assay Kit (R&D Systems) according to manufacturer's instructions.

PGEM measurement

Mouse tracheas were cleaned, rinsed in cold PBS containing 7.5 μg/mL indomethacin, and snap-frozen. Frozen samples were homogenized in indomethacin-containing PBS, and debris was removed by centrifugation at 12,000g, for 10 minutes, at 4°C. Lysates underwent acetone precipitation and derivation and were assayed according to manufacturer's instructions for Prostaglandin E Metabolite ELISA Kit (Cayman Chemical).

Imaging

Organoids were imaged on an inverted Nikon A1R with DS-Fi3 camera or upright light microscope (Leica). Manual measurements of organoids at estimated maximal diameter were performed on NIS Elements or Fiji software.

For immunofluorescence of mouse tissue, 4% paraformaldehyde-fixed, sucrose-protected anterior skulls were embedded in optimal cutting media (OCT, Sakura Finetek) and cryosectioned at 8 μm thickness midway between the incisors and nares. For whole-mount tracheas, entire fixed tracheas were filleted open and cleaned of attached connective tissue. Tissues were stained for DCLK1 (Abcam catalog ab31704) and RFP (SICGEN, catalog AB8181) followed by appropriate secondaries, counterstained with DAPI, mounted, and analyzed on a Nikon A1R confocal microscope using NIS Elements (Nikon) and Fiji (ImageJ, NIH) software.

For particle transport measurements, 20 μL of 5 μm fluorescently labeled polystyrene beads (Bang's Laboratories) in PBS was applied to the center of the apical surface of human tracheal epithelia on Transwell inserts and PGE$_2$ (1 μg/mL) with/without CFTR inhibitor 172 (10 μM) applied on the basolateral side. After 1 hour in a standard tissue culture incubator, tissue culture plates were transferred to a 37°C, 5% CO$_2$-injected incubated stage of a Nikon A1R confocal microscope, and 30-second videos were obtained for each well. Track speeds for individual particles were calculated using Imaris 9.7.2 software. Track speeds were log-transformed to obtain a normal data distribution before testing by 1-way ANOVA.

RNAscope multiplex fluorescence in situ hybridization

Human sinus tissues were fixed in 10% neutral buffered formalin and embedded in paraffin. Paraffin blocks were sectioned onto glass microscope slides, dried overnight, and baked for 1 hour at 60°C before immediately proceeding with the RNAscope Multiplex Fluorescent v2 assay according to the manufacturer's protocol (Advanced Cell Diagnostics). Deparaffinization was performed with 100% xylene followed by

100% ethanol. The tissue sections were pretreated with RNAscope Hydrogen Peroxide, followed by target retrieval and Protease plus pretreatment. Pretreated sections were hybridized with target probes *POU2F3* or *FOXI1* for 2 hours at 40°C. Hybridized slides were left overnight in 5XSSC before proceeding with the amplification and labeling steps. Targeted probes were labeled with Opal dyes (1:500, Akaya Biosciences), and cell-cell junctions were visualized with E-cadherin antibody (1:2000; ECM biosciences catalog CM1681, clone M168) followed by Alexa fluorochrome–conjugated donkey anti-mouse IgG (1:500, Thermo Fisher Scientific, catalog A32787). For nuclear staining, sections were incubated with DAPI for 5 minutes at room temperature. All stained sections were mounted with ProLong Diamond Mount Medium (Invitrogen) and imaged on an Echo Revolve R4 fluorescence microscope.

Data and materials availability
Single-cell RNA-Seq data have been deposited at the NCBI GEO under accession number GSE202100. Code used to carry out data analysis is available upon request.

Statistics
Statistical methods used for single-cell and bulk sequencing analysis of human participants are described in detail in the corresponding subsections of the Methods and figure legends. Specific statistical comparisons (with corrections for multiple comparisons) relating to Figure 2 are included in Supplemental Table 7. For mouse studies, a power calculation was made whenever possible based on pilot studies to determine the number of mice needed to detect what we considered a biologically meaningful difference. For mouse studies, 2-tailed *t* testing or 1-way ANOVA was performed in GraphPad Prism, or nonparametric tests were performed as indicated in figure legends. *P* less than 0.05 was considered statistically significant.

Study approval
Sampling from human participants was approved by the UCSF Committee on Human Research, and all participants provided written informed consent. All experimental procedures on mice were approved by the UCSF Institutional Animal Care and Use Committee.

Author contributions
MEK, CMM, JGG, SDP, ANG, RA, SY, PEB, CAS, PLZ, IHZ, YL, MTM, KL, EKC, RML, MAS, and EDG substantially contributed to the acquisition, analysis, or interpretation of data for the manuscript and drafting, revising, and critically reviewing the manuscript for important intellectual content. MEK, EKC, RML, MAS, and EDG conceptualized the experiments. JGG, SDP, and ANG recruited participants and obtained epithelial brushes. MEK, CMM, RA, SY, MTM, CAS, IHZ, YL, KL, and EDG performed experiments and analyzed data. MEK, CMM, MAS, and EDG synthesized the data and drafted the manuscript, which was further edited by MEK, CMM, RML, MAS, and EDG. All authors approved the final version of this manuscript.

Acknowledgments

Address correspondence to: Erin D. Gordon, Division of Pulmonary, Critical Care, Allergy and Sleep Medicine, Department of Medicine, University of California, San Francisco, HSE 201, 513 Parnassus Ave., San Francisco, California 94143, USA. Phone: 415.476.9456; Email: erin.gordon@ucsf.edu. Or to: Max A. Seibold, Center for Genes, Environment, and Health, National Jewish Health, University of Colorado-AMC, School of Medicine, Smith Building A648, 1400 Jackson Street, Denver, Colorado 80206, USA. Phone: 303.270.2544; Email: seiboldm@njhealth.org.

1. Kristjansson RP, et al. A loss-of-function variant in ALOX15 protects against nasal polyps and chronic rhinosinusitis. *Nat Genet*. 2019;51(2):267–276.

2. Moffatt MF, et al. A large-scale, consortium-based genomewide association study of asthma. *N Engl J Med*. 2010;363(13):1211–1221.

3. Jarvis D, et al. Asthma in adults and its association with chronic rhinosinusitis: the GA2LEN survey in Europe. *Allergy*. 2012;67(1):91–98.

4. Jackson ND, et al. Single-cell and population transcriptomics reveal pan-epithelial remodeling in type 2-high asthma. *Cell Rep*. 2020;32(1):107872.

5. Plasschaert LW, et al. A single-cell atlas of the airway epithelium reveals the CFTR-rich pulmonary ionocyte. *Nature*. 2018;560(7718):377–381.

6. Montoro DT, et al. A revised airway epithelial hierarchy includes CFTR-expressing ionocytes. *Nature*. 2018;560(7718):319–324.

7. Shivaraju M, et al. Airway stem cells sense hypoxia and differentiate into protective solitary neuroendocrine cells. *Science*. 2021;371(6524):52–57.

8. Sui P, et al. Pulmonary neuroendocrine cells amplify allergic asthma responses. *Science*. 2018;360(6393):eaan8546.

9. Gerbe F, et al. Intestinal epithelial tuft cells initiate type 2 mucosal immunity to helminth parasites. *Nature*. 2016;529(7585):226–230.

10. Von Moltke J, et al. Tuft-cell-derived IL-25 regulates an intestinal ILC2-epithelial response circuit. *Nature*. 2016;529(7585):221–225.

11. Howitt MR, et al. Tuft cells, taste-chemosensory cells, orchestrate parasite type 2 immunity in the gut. *Science*. 2016;351(6279):1329–1333.

12. Tizzano M, et al. Nasal chemosensory cells use bitter taste signaling to detect irritants and bacterial signals. *Proc Natl Acad Sci U S A*. 2010;107(7):3210–3215.

13. Bankova LG, et al. The cysteinyl leukotriene 3 receptor regulates expansion of IL-25-producing airway brush cells leading to type 2 inflammation. *Sci Immunol*. 2018;3(28):eaat9453.

14. Kohanski MA, et al. Solitary chemosensory cells are a primary epithelial source of IL-25 in patients with chronic rhinosinusitis with nasal polyps. *J Allergy Clin Immunol*. 2018;142(2):460–469.

15. Patel NN, et al. Solitary chemosensory cells producing interleukin-25 and group-2 innate lymphoid cells are enriched in chronic rhinosinusitis with nasal polyps. *Int Forum Allergy Rhinol*. 2018;8(8):900–906.

16. Ordovas-Montanes J, et al. Allergic inflammatory memory in human respiratory epithelial progenitor cells. *Nature*. 2018;560(7720):649–654.

17. Vieira Braga FA, et al. A cellular census of human lungs identifies novel cell states in health and in asthma. *Nat Med*. 2019;25(7):1153–1163.

18. Zhang Y, et al. Th2 cytokines orchestrate the secretion of MUC5AC and MUC5B in IL-5-positive chronic rhinosinusitis with nasal polyps. *Allergy*. 2019;74(1):131–140.

19. Goldfarbmuren KC, et al. Dissecting the cellular specificity of smoking effects and reconstructing lineages in the human airway epithelium. *Nat Commun*. 2020;11(1):2485.

20. Deprez M, et al. A single-cell atlas of the human healthy airways. *Am J Respir Crit Care Med*. 2020;202(12):1636–1645.

21. Nadjsombati MS, et al. Detection of succinate by intestinal tuft cells triggers a type 2 innate immune circuit. *Immunity*. 2018;49(1):33–41.

22. Haber AL, et al. A single-cell survey of the small intestinal epithelium. *Nature*. 2017;551(7680):333–339.

23. Woodruff PG, et al. Genome-wide profiling identifies epithelial cell genes associated with asthma and with treatment response to corticosteroids. *Proc Natl Acad Sci U S A*. 2007;104(40):15858–15863.

24. Poole A, et al. Dissecting childhood asthma with nasal transcriptomics distinguishes subphenotypes of disease. *J Allergy Clin Immunol*. 2014;133(3):670–678.

25. Klapan I, et al. Arachidonic acid metabolites and sinonasal polyposis. I. Possible prognostic value. *Am J Otolaryngol*. 1995;16(6):396–402.

26. Joshi R, et al. Prostanoid receptors of the EP_4-subtype mediate gene expression changes in human airway epithelial cells with potential anti-inflammatory activity. *J Pharmacol Exp Ther*. 2021;376(2):161–180.

27. Fujii S, et al. PGE_2 is a direct and robust mediator of anion/fluid secretion by human intestinal epithelial cells. *Sci Rep*. 2016;6:36795.

28. Miyoshi H, et al. Prostaglandin E2 promotes intestinal repair through an adaptive cellular response of the epithelium. *EMBO J*. 2017;36(1):5–24.

29. Muraglia KA, et al. Small-molecule ion channels increase host defences in cystic fibrosis airway epithelia. *Nature*. 2019;567(7748):405–408.

30. Matsui H, et al. Evidence for periciliary liquid layer depletion, not abnormal ion composition, in the pathogenesis of cystic fibrosis airways disease. *Cell*. 1998;95(7):1005–1015.

31. Shah VS, et al. Airway acidification initiates host defense abnormalities in cystic fibrosis mice. *Science*. 2016;351(6272):503–507.

32. Bonser LR, et al. Epithelial tethering of MUC5AC-rich mucus impairs mucociliary transport in asthma. *J Clin Invest*. 2016;126(6):2367–2371.

33. Dunican EM, et al. Mucus plugs in patients with asthma linked to eosinophilia and airflow obstruction. *J Clin Invest*.

2018;128(3):997–1009.

34. Meth MJ, et al. High frequency of CF transmembrane conductance regulator (CFTR) mutations in a population with persistent asthma and/or chronic rhinosinusitis. *J Allergy Clin Immunol*. 2009;123(2):S159.

35. Dwyer DF, et al. Human airway mast cells proliferate and acquire distinct inflammation-driven phenotypes during type 2 inflammation. *Sci Immunol*. 2021;6(56):eabb7221.

36. Dougherty RH, et al. Accumulation of intraepithelial mast cells with a unique protease phenotype in T(H)2-high asthma. *J Allergy Clin Immunol*. 2010;125(5):1046–1053.

37. Watts AM, et al. Adult allergic rhinitis sufferers have unique nasal mucosal and peripheral blood immune gene expression profiles: a case-control study. *Immun Inflamm Dis*. 2022;10(1):78–92.

38. Williams TJ, Peck MJ. Role of prostaglandin-mediated vasodilatation in inflammation. *Nature*. 1977;270(5637):530–532.

39. Harris SG, et al. Prostaglandins as modulators of immunity. *Trends Immunol*. 2002;23(3):144–150.

40. Zhang Y, et al. Tissue regeneration. Inhibition of the prostaglandin-degrading enzyme 15-PGDH potentiates tissue regeneration. *Science*. 2015;348(6240):aaa2340.

41. Langenbach R, et al. Prostaglandin synthase 1 gene disruption in mice reduces arachidonic acid-induced inflammation and indomethacin-induced gastric ulceration. *Cell*. 1995;83(3):483–492.

42. Oshima M, et al. Suppression of intestinal polyposis in Apc delta716 knockout mice by inhibition of cyclooxygenase 2 (COX-2). *Cell*. 1996;87(5):803–809.

43. Arber N, et al. Celecoxib for the prevention of colorectal adenomatous polyps. *N Engl J Med*. 2006;355(9):885–895.

44. Roulis M, et al. Paracrine orchestration of intestinal tumorigenesis by a mesenchymal niche. *Nature*. 2020;580(7804):524–529.

45. Chang WM, et al. Parathyroid hormone-like hormone is a poor prognosis marker of head and neck cancer and promotes cell growth via RUNX2 regulation. *Sci Rep*. 2017;7(1):41131.

46. Varma Shrivastav S, et al. Insulin-like growth factor binding protein-3 (igfbp-3): unraveling the role in mediating IGF-independent effects within the cell. *Front Cell Dev Biol*. 2020;8:286.

47. Ellen TP, et al. NDRG1, a growth and cancer related gene: regulation of gene expression and function in normal and disease states. *Carcinogenesis*. 2008;29(1):2–8.

48. Huang YH, et al. POU2F3 is a master regulator of a tuft cell-like variant of small cell lung cancer. *Genes Dev*. 2018;32(13–14):915–928.

49. Kunze B, et al. Notch signaling drives development of Barrett's metaplasia from Dclk1-positive epithelial tuft cells in the murine gastric mucosa. *Sci Rep*. 2021;11(1):4509.

50. Yamada Y, et al. A tuft cell-like signature is highly prevalent in thymic squamous cell carcinoma and delineates new molecular subsets among the major lung cancer histotypes. *J Thorac Oncol*. 2021;16(6):1003–1016.

51. Goto N, et al. Lineage tracing and targeting of IL17RB+ tuft cell-like human colorectal cancer stem cells. *Proc Natl Acad Sci U S A*. 2019;116(26):12996–13005.

52. Bachert C, et al. Efficacy and safety of dupilumab in patients with severe chronic rhinosinusitis with nasal polyps (LIBERTY NP SINUS-24 and LIBERTY NP SINUS-52): results from two multicentre, randomised, double-blind, placebo-controlled, parallel-group phase 3 trials. *Lancet*. 2019;394(10209):1638–1650.

53. Lee TH. Mechanism of aspirin sensitivity. *Am Rev Respir Dis*. 1992;145(2 pt 2):S34–S36.

54. Cahill KN, et al. Impaired E prostanoid2 expression and resistance to prostaglandin E2 in nasal polyp fibroblasts from subjects with aspirin-exacerbated respiratory disease. *Am J Respir Cell Mol Biol*. 2016;54(1):34–40.

55. Butler A, et al. Integrating single-cell transcriptomic data across different conditions, technologies, and species. *Nat Biotechnol*. 2018;36(5):411–420.

56. Stuart T, et al. Comprehensive integration of single-cell data. *Cell*. 2019;177(7):1888–1902.

57. McInnes L, et al. UMAP: uniform manifold approximation and projection for dimension reduction. https://arxiv.org/abs/1802.03426. Accessed May 31, 2022.

58. Lun AT, et al. A step-by-step workflow for low-level analysis of single-cell RNA-seq data with Bioconductor. *F1000Res*. 2016;5:2122.

59. Bach K, et al. Differentiation dynamics of mammary epithelial cells revealed by single-cell RNA sequencing. *Nat Commun*. 2017;8(1):2128.

60. Bais AS, Kostka D. scds: computational annotation of doublets in single-cell RNA sequencing data. *Bioinformatics*. 2020;36(4):1150–1158.

61. Crowell HL, et al. muscat detects subpopulation-specific state transitions from multi-sample multi-condition single-cell transcriptomics data. *Nat Commun*. 2020;11(1):6077.

62. Lun ATL, Marioni JC. Overcoming confounding plate effects in differential expression analyses of single-cell RNA-seq data. *Biostatistics*. 2017;18(3):451–464.

63. Zimmerman KD, et al. A practical solution to pseudoreplication bias in single-cell studies. *Nat Commun*. 2021;12(1):738.

64. Robinson MD, et al. edgeR: a Bioconductor package for differential expression analysis of digital gene expression data. *Bioinformatics*. 2010;26(1):139–140.

65. McCarthy DJ, et al. Differential expression analysis of multifactor RNA-Seq experiments with respect to biological variation. *Nucleic Acids Res*. 2012;40(10):4288–4297.

66. Benjamini Y, et al. Controlling the false discovery rate in behavior genetics research. *Behav Brain Res*. 2001;125(1–2):279–284.

67. Kuznetsova A, et al. lmerTest package: tests in linear mixed effects models. *J Stat Softw*. 2017;82(13).

68. Bates D, et al. Fitting linear mixed-effects models using lme4. *J Stat Softw*. 2015;67(1).

69. Love MI, et al. Moderated estimation of fold change and dispersion for RNA-seq data with DESeq2. *Genome Biol*. 2014;15(12):550.

70. Yamaya M, et al. Differentiated structure and function of cultures from human tracheal epithelium. *Am J Physiol*. 1992;262(6 pt 1):L713–L724.

71. Reynolds SD, et al. Airway progenitor clone formation is enhanced by Y-27632-dependent changes in the transcriptome. *Am J Respir Cell Mol Biol*. 2016;55(3):323–336.

72. Schneider C, et al. A metabolite-triggered tuft cell-ILC2 circuit drives small intestinal remodeling. *Cell*. 2018;174(2):271–284.